Strong Adaptability Control Based on Dual-Division-Summation Current Control for an *LCL*-Type Grid-Connected Inverter

Jiang Liu, Xiangdong Sun, *Member, IEEE*, Biying Ren, Weizhang Song, and Patrick Wheeler, *Fellow, IEEE*

***Abstract*—The nonignorable grid impedance is one of the characteristics of a weak grid. Meanwhile, the filter inductance also fluctuates with temperature or aging factors. The resonant frequency offset of an *LCL* filter will be caused by the change in power grid impedance and filter inductance. To this end, a strong adaptability control based on dual-division-summation (D-D-Σ) control is proposed in this article, which considers both the accuracy of grid-connected current tracking and resonance suppression under the variation of grid impedance and filter inductance. A full inductance parameter identification method based on an extended Kalman filter for simultaneously estimating filter inductance and grid impedance is proposed without remote voltage sampling. An enumeration method of the Routh array with less calculation is proposed. The algebraic relationship between control parameters and total inductance parameters is obtained by the Routh criterion. A gain correction method to realize strong adaptive control is proposed to deal with the variation of grid impedance and filter inductance. The experimental results prove the feasibility of D-D-Σ control in a three-phase *LCL*-type grid-connected inverter under the variation of grid impedance and filter inductance.**

***Index Terms*—DC AC power converters, electric current control, kalman filters, stability criteria.**

I. Introduction

THE grid-connected inverter is the power electronic interface between a distributed power generation system and the power grid. To improve the robustness of the power grid, an *LCL* filter is usually used to filter the high-order harmonics in the grid current. The *LCL* filter has a smaller inductance value, better high-frequency harmonic suppression effect, and higher power density than an *L* filter. However, the inverter with the *LCL* filter is subjected to an instability issue, which will result in grid-current distortion [1]–[3].

Although the *LCL* filter can filter out the high-order harmonics, the harmonics injection caused by the control method and modulation strategy should be considered. Conventionally, the voltage source inverters are modulated with sinusoidal pulsewidth modulation (SPWM) or space vector pulsewidth modulation and are controlled by various control methods. The common grid-connected current control methods are proportional-integral control in the *dq* frame [4], [5] and proportional-resonant control in the $\alpha\beta$ frame [6], [7]. These two control methods need coordinate transformation, which transforms the control variables in *abc* frame to *dq* or $\alpha\beta$ frame. Model predictive current control [8], [9] was proposed to improve the anti-interference ability of the system, but the improvement of switching frequency is very important. One cycle control [10] used the dual-buck concept to derive the control law without the coordinate transformation. However, inductance current variation levels have not been considered in the controller design yet. Deadbeat control [11], [12] established the system dynamics model and its state equation and then used the system parameters, load changes, and error signals to operate the state equation so that the error current signal could be compensated in the next switching cycle. Hysteretic control [13], [14] was a simple structure without closed-loop compensation. But its filter design is difficult due to varying switching frequencies. Other control methods also provided some current control schemes, such as direct power control [15], [16], model-based current control [17], and weighted average current control [18]. Researchers proposed a division-summation (D-Σ) digital control to cover wide inductance variation and to track sinusoidal inverter current reference precisely [19]. D-Σ digital control can overcome the limitations of the conventional *abc* to *dq* frame transformation and cover the effect of wide filter-inductance variation. Then, the applications of D-Σ digital control are reported, such as applications in single-phase [20] and three-phase inverters [21], surface-mounted permanent-magnet synchronous generators [22], active power filters [23], three-phase back-to-back transformerless inverters [24], and bidirectional grid-connected modular multilevel converters [25]. All these references verify the feasibility and superiority of D-Σ digital control. However, most of the references about D-Σ digital control are in an *LC*-type inverter. The applications of D-Σ digital control in an *LCL*-type inverter are relatively less. Since

Manuscript received 22 March 2022; revised 24 May 2022; accepted 1 July 2022. Date of publication 5 July 2022; date of current version 6 September 2022. This work was supported in part by the National Natural Science Foundation of China under Grant 51577155 and Grant 51877176, in part by the Natural Science Foundation of Shaanxi Province under Grant 2018JZ5006, and in part by the Education Service Local Special Plan Project of Shaanxi Provincial Department under Grant 18JC024. Recommended for publication by Associate Editor B. Mirafzal. *(Corresponding author: Xiangdong Sun.)*

Jiang Liu, Xiangdong Sun, Biying Ren, and Weizhang Song are with the Department of Electrical Engineering, Xi'an University of Technology, Xi'an 710048, China (e-mail: lj15667083657@126.com; sxd1030@163.com; renby@126.com; songwz464237@126.com).

Patrick Wheeler is with the Department of Electrical Engineering, University of Nottingham, Nottingham NG7 2RD, U.K. (e-mail: pat.wheeler@nottingham.ac.uk).

Color versions of one or more figures in this article are available at https://doi.org/10.1109/TPEL.2022.3188562.

Digital Object Identifier 10.1109/TPEL.2022.3188562

there typically exist grid voltage harmonics, the injected grid current will contain harmonic components due to the effect of the *LCL* filter capacitance. For the research of the *LCL* inverter, resonance suppression is an inevitable problem. In [26], the low-frequency and high-frequency components of capacitive current are filtered by filter-capacitance current compensation (FCCC) and *RC* damping, respectively. However, the descriptions of the capacitance-current-feedback coefficient and the selection of damping parameters are vague. Wu *et al.* [20] applied the D-Σ control method to an *LCL*-type grid-connected inverter for the first time. Compared with *LC*-type inverters, *LCL*-type grid-connected inverters are characterized by resonance suppression. The FCCC method is selected for resonance suppression in [20]. The current control laws under rectification and grid-connection modes are deduced. In terms of suppressing the resonance effect, a very ingenious design is proposed in [20]. Comparing an *LCL* filter with an *LC* filter, the inductor current at the inverter side of the *LCL* filter is equivalent to the inductor current in the *LC* filter. Then, the inductor current reference at the inverter side of the *LCL* filter is the sum of the fundamental sinusoidal current and the filter capacitor current. The filter capacitor current is obtained by integrating the capacitor voltage. The capacitor voltage is the sum of the point of common coupling (PCC) voltage and inductor voltage on the grid side of the *LCL* filter. In general, when the capacitance current compensation method is used to suppress the resonance, it can be found from the control block diagram that the capacitance current is obtained by subtracting the grid-connected current from the inductance current on the inverter side [27], [28]. The method in [20] reduces the number of sampling channels. However, the D-Σ control method is a digital control method considering the variation of inductor current. The method in [20] does not fully consider the current variation of the two inductors. As a result, the dual-division-summation (D-D-Σ) digital control is proposed in this article, which considers the accuracy of grid-connected current tracking and resonance suppression simultaneously.

Generally speaking, the nonignorable grid impedance under a weak grid affects the resonant frequency of an *LCL* filter. A grid-connected inverter requires higher stability under a weak grid. In [29], the variation of gird impedance is considered, and a model reference adaptive state feedback control is employed to guarantee the system stability. Its disadvantage is that it needs more sampling circuits to realize. He *et al.* [30] proposed an active grid impedance cancelator to suppress the effect of the grid disturbance and stabilize the single-phase grid-connected inverters with an inductive capacitive inductive filter operating under variable grid conditions. However, the grid impedance is considered unknown and variable. In [31], the coupling relationship between phase-locked loop (PLL) and grid impedance is revealed. A decoupling method is proposed to improve the stability of the system. A simplified full feedforward strategy based on grid-side inductor voltage differential feedback active damping is proposed and a virtual impedance branch is added to meet the stability requirements of the inverter when the grid impedance changes suddenly [32]. These references do not consider the online parameter estimation method to obtain accurate real-time parameters of grid impedance. The online estimation method of grid impedance has been reported in some references. For example, pulse injection [33], orthogonal binary sequence [34], and discrete interval binary sequence [35] realize online grid or inverter impedance measurement for stability evaluation. In [36], the EKF is proposed to estimate the grid impedance online, which avoids additional harmonic injection. However, these grid impedance estimation methods do not consider the filter inductance parameters, which also affects the stability of the system. To this end, a full inductance parameter estimation method based on EKF is proposed in this article, which does not require remote voltage sampling. The proposed method can estimate the changes in filter inductance and grid impedance at the same time.

Thus, the main contributions of this article are as follows.

1) Based on D-Σ digital control, a D-D-Σ digital control is proposed to consider both the accuracy of grid-connected current tracking and resonance suppression simultaneously. The D-D-Σ digital control is used to deduce the control laws of inverter-side current and grid-connected current, which avoids the complicated coordinate transformation.
2) To adapt to the wide range variation of filter inductance and grid inductance under a weak grid, an *RC* is chosen as the stability criterion of the three-phase inverter. The demonstration of the adaptability of D-D-Σ current control to a wide range of variations of inductance is quantified. The correctness of the stability analysis is proved by the Bode diagram of the open-loop transfer function.
3) A full inductance parameter estimation method based on EKF is proposed in this article. The proposed EKF only needs the gird-connected current, which reduces the number of sampling channels. The inductance estimation method considers not only the grid impedance under the weak grid but also the fluctuation of the filter inductance.
4) Based on the proposed D-D-Σ current control, a gain correction method is proposed to deal with the variation of filter inductance and grid impedance. The gain correction method can still ensure the grid current tracking accuracy and inverter stability.

Driven by this urgent demand, a strong adaptability control based on D-D-Σ current control is proposed in this article, which can improve the stability of grid-connected inverter systems under the variation of filter inductance and grid impedance. This article consists of the following sections. Section II derives the grid-connected current control method based on D-D-Σ digital control in detail. In Section III, *RC* is introduced as a stability criterion to quantify the adaptability of D-D-Σ digital control. In Section IV, a full inductance parameter estimation method based on EKF and a gain correction method is proposed to cope with a wide range of variations of filter inductance and grid impedance. Section V presents the experimental verification and analysis. Section VI concludes this article.

II. Review of D-D-Σ Current Control

The circuit topology of a T-type three-level grid-connected inverter with the *LCL* filter is shown in Fig. 1. The voltages of upper and lower capacitors on the dc side are u_{C1} and u_{C2}, respectively. U_{dc} is a dc input voltage, and $U_{\mathrm{PCC}x}$ represents the

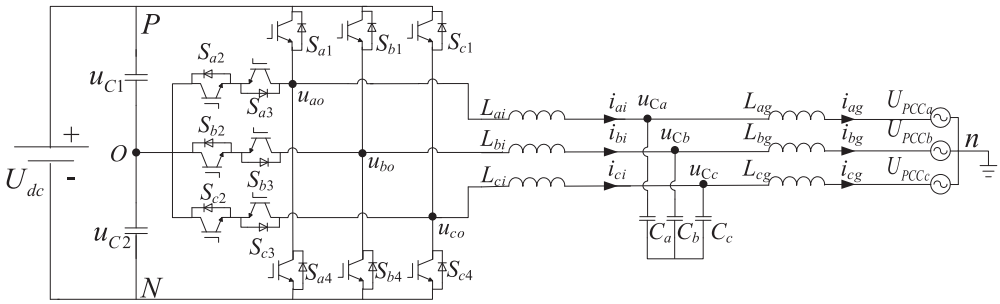

Fig. 1. Circuit topology of the T-type three-level grid-connected inverter with the *LCL* filter.

voltage at the PCC. The output voltage of the inverter is represented by u_{xo}. The inverter-side inductance L_{xi}, capacitance C_x, and grid-side inductance L_{xg} constitute the *LCL* filter; $x = a, b, c$. Note that the grid-side inductance L_{xg} here does not include the grid impedance.

According to Kirchhoff's voltage law, the mathematical model of the T-type three-level grid-connected inverter with the *LCL* filter in the *abc* frame can be listed as

$$\begin{cases} L_{xi}\dfrac{di_{xi}}{dt} = u_{xo} - u_{Cx} \\ C_x\dfrac{du_{cx}}{dt} = i_{xi} - i_{xg} \\ L_{xg}\dfrac{di_{xg}}{dt} = u_{Cx} - U_{\mathrm{PCC}x} \end{cases}, \ x = a, b, c \tag{1}$$

where i_{xi} and i_{xg} represent inverter-side and grid-side inductance currents, respectively, and u_{Cx} represents the voltage of filter capacitance.

Equation (1) can be converted into

$$u_{xo} = L_{xi}\frac{di_{xi}}{dt} + L_{xg}\frac{di_{xg}}{dt} + U_{\mathrm{PCC}x}, \ \ x = a, b, c. \tag{2}$$

Within a half cycle of the modulation wave, (2) for half switching cycle under the balanced dc-side voltage can be written as

$$L_{xg}\frac{di_{xg}}{dt} + L_{xi}\frac{di_{xi}}{dt} = \begin{cases} \dfrac{U_{\mathrm{dc}}}{2} - U_{\mathrm{PCC}x}, \ t \in (n, n + t_{\mathrm{Pon}}) \\ -U_{\mathrm{PCC}x}, \ t \in (n + t_{\mathrm{Pon}}, \ n + \dfrac{1}{2}) \\ -\dfrac{U_{\mathrm{dc}}}{2} - U_{\mathrm{PCC}x}, \ t \in (n + \dfrac{1}{2}, \ n + \frac{1}{2} + t_{\mathrm{Non}}) \\ -U_{\mathrm{PCC}x}, \ t \in (n + \dfrac{1}{2} + t_{\mathrm{Non}}, \ n + 1) \end{cases} \tag{3}$$

where n represents the sampling time. t_{Pon} represents the action time of $+U_{\mathrm{dc}}/2$. t_{Non} represents the action time of $-U_{\mathrm{dc}}/2$. $+U_{\mathrm{dc}}/2$ means that the modulation wave is within the positive half-period. $-U_{\mathrm{dc}}/2$ means that the modulation wave is within the negative half-period. $x = a, b, c$.

The inverter output voltage includes three working states $+U_{\mathrm{dc}}/2$, 0, and $-U_{\mathrm{dc}}/2$. Thus, the duty ratios corresponding to $+U_{\mathrm{dc}}/2$ (P), 0 (O), and $-U_{\mathrm{dc}}/2$ (N) can be set to

$$\begin{cases} d_{xP} = d_x \\ d_{xO} = 1 - 2d_x \\ d_{xN} = -d_x \end{cases} \tag{4}$$

where d_x represents the duty ratio when the output voltage is $+U_{\mathrm{dc}}/2$; $x = a, b, c$. Because of the symmetry of the output waveform, when the output voltage is $-U_{\mathrm{dc}}/2$, the duty cycle is $-d_x$.

According to [37], since the amplitude of the capacitor current is relatively small, it is assumed that the fundamental reference currents of the two inductors of the *LCL* filter are equal. The proposed D-D-Σ digital control needs additional consideration of resonance suppression. When the resonance suppression effect reaches its best, the fundamental current flowing through the filter capacitor is almost zero. Therefore, it can be considered that the fundamental inductor current on the inverter side is consistent with the grid-connected current

$$I_{xg\mathrm{ref}}(n+1) = I_{xi\mathrm{ref}}(n+1) \tag{5}$$

where $I_{xg\mathrm{ref}}(n+1)$ and $I_{xi\mathrm{ref}}(n+1)$ are the reference values of grid-connected current and inverter-side inductance current at the $(n+1)$th switching period, respectively.

A. Dual Division

The dual division of the inverter-side inductor current and grid-connected current can be obtained as

$$\begin{cases} 2L_{xg}\Delta i_{xgP+} + 2L_{xi}\Delta i_{xiP+} = \left(\dfrac{U_{\mathrm{dc}}}{2} - U_{\mathrm{PCC}x}\right) d_x T_s \\ 2L_{xg}\Delta i_{xgO-} + 2L_{xi}\Delta i_{xiO-} = -\left(-\dfrac{U_{\mathrm{dc}}}{2} - U_{\mathrm{PCC}x}\right) d_x T_s \\ 2L_{xg}\Delta i_{xgO+} + 2L_{xi}\Delta i_{xiO+} = -(1 - d_x)\, T_s U_{\mathrm{PCC}x} \\ 2L_{xg}\Delta i_{xgP-} + 2L_{xi}\Delta i_{xiP-} = -(1 + d_x)\, T_s U_{\mathrm{PCC}x} \\ \Delta i_{xgN+} = \Delta i_{xiN+} = 0 \\ \Delta i_{xgP-} = \Delta i_{xiP-} = 0 \end{cases} \tag{6}$$

where Δi_{xyz+} represents current variation corresponding to working state z of phase x on y-side inductance under positive half cycle. Δi_{xyz-} represents current variation corresponding to working state z of phase x on y-side inductance under negative half cycle ($x = a, b, c$; $y = i$ (inverter); and g (grid). $z = P, O, N$).

B. Summation

By summarizing (6), the total current change of the positive half cycle and the negative half cycle can be expressed as

$$2L_{xg}\left(\Delta i_{xg+} + \Delta i_{xg-}\right) + 2L_{xi}\left(\Delta i_{xi+} + \Delta i_{xi-}\right)$$

$$= 2L_{xg}\Delta i_{xg} + 2L_{xi}\Delta i_{xi}$$
$$= U_{\rm dc} d_x T_s - 2T_s U_{{\rm PCC}x} \quad (7)$$

where Δi_{xy} represents the current variation of phase x on y-side inductance under a complete cycle.

Thus, the duty ratio expression of the grid-connected current in a complete cycle can be deduced to

$$d_x = \frac{2L_{xg}\Delta i_{xg} + 2L_{xi}\Delta i_{xi} + 2T_s U_{{\rm PCC}x}}{U_{\rm dc} T_s}. \quad (8)$$

As described in [20], $I_{x\rm ref}(n+1) - i_x(n)$ can be used instead of the two inductance current variations

$$d_x = \frac{2L_{xi}\left[I_{xi\rm ref}(n+1) - i_{xi}(n)\right]}{U_{\rm dc} T_s} + \frac{2L_{xg}\left[I_{xg\rm ref}(n+1) - i_{xg}(n)\right]}{U_{\rm dc} T_s} + \frac{2U_{{\rm PCC}x}}{U_{\rm dc}} \quad (9)$$

where $i_{xg}(n)$ and $i_{xi}(n)$ are the sampling values of grid-connected current and inverter-side inductance current at the nth switching period, respectively.

Therefore, the reference value of inverter-side inductance can be replaced by that of grid-connected current. Equation (9) can be converted into

$$d_x = \frac{2L_{xi}\left[I_{xg\rm ref}(n+1) - i_{xi}(n)\right]}{U_{\rm dc} T_s} + \frac{2L_{xg}\left[I_{xg\rm ref}(n+1) - i_{xg}(n)\right]}{U_{\rm dc} T_s} + \frac{2U_{{\rm PCC}x}}{U_{\rm dc}}. \quad (10)$$

By changing (10) appropriately, the following equation can be obtained

$$d_x = K_{p1}\left[I_{xg\rm ref}(n+1) - i_{xi}(n)\right] + K_{p2}\left[I_{xg\rm ref}(n+1) - i_{xg}(n)\right] + K_{p3} U_{{\rm PCC}x} \quad (11)$$

where $K_{p1} = 2L_{xi}/(U_{\rm dc}T_{\rm s})$, $K_{p2} = 2L_{xg}/(U_{\rm dc}T_s)$, and $K_{p3} = 2/(U_{\rm dc}T_s)$.

In (11), K_{p2} represents the grid-connected current control gain, which affects the current tracking accuracy. K_{p1} represents the inverter-side inductance current control gain, which affects the resonance suppression effect. K_{p3} represents the feedforward gain of grid voltage at PCC. Through the derivation process, D-D-Σ digital control is a three-phase current independent control without coordinate transformation. Therefore, when the three phases are unbalanced, the balanced three-phase grid current can still be obtained under D-D-Σ digital control. With the control law based on the D-D-Σ digital control, the grid-connected current can track the reference precisely by cycle to yield the sinusoidal grid-connected current. The configuration of D-D-Σ digital control is depicted in Fig. 2. The PLL provides the phase of grid voltage at PCC to ensure the reference current in synchronization with the grid voltage. The grid-connected current feedback is the outer current close loop to trace the reference current. Besides, the inverter-side current feedback is the inner loop to improve the resonance suppression effect. The PCC voltage feedback through feedback parameter K_{p3} is feedforwarded to reduce the influence of PCC. Total controls are in the *abc* coordinate. Finally, the signal is modulated by an SPWM strategy to gate drivers in switches.

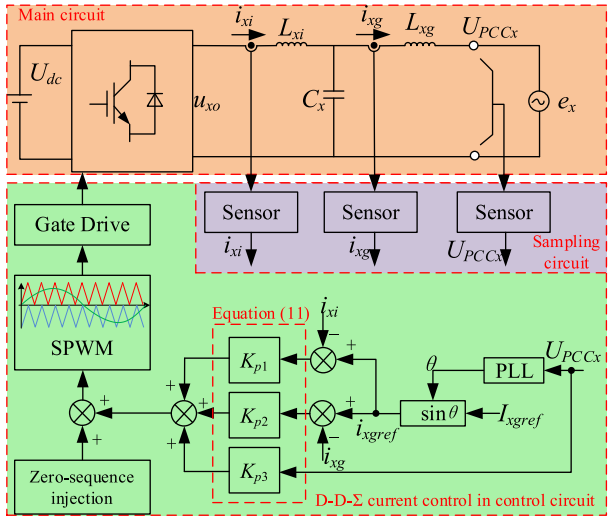

Fig. 2. Configuration of D-D-Σ digital control.

III. Adaptive Ability for Wide Range Variation of Grid Inductance in Weak Grid

According to (11), the current control block diagram based on D-D-Σ digital control can be illustrated in Fig. 3. Note that $U_{{\rm PCC}x}$ in (11) can be considered as a disturbance term. The feedforward term of grid voltage can improve the antidisturbance ability of the system. In Fig. 3, $G_{\rm inv}$ is the transfer gain of the inverter. In general, $G_{\rm inv}$ is the product of delay link G_d and $K_{\rm pwm}$ [38].

According to Fig. 3, the closed-loop transfer function of the system can be expressed in (12) shown at the bottom of this page.

By using the two bilinear transformation equations of $s = (2/T_s)[(z-1)/(z+1)]$ and $z = (w+1)/(1-w)$, $G_{\rm close}(s)$ in s-domain is transformed to that in w-domain [39], [40]

$$G_{\rm close}(w) = \frac{T_s^3\left(K_{p1}+K_{p2}\right)w^4 - T_s^3\left(K_{p1}+K_{p2}\right)w^3}{a_0 w^4 + a_1 w^3 + a_2 w^2 + a_3 w^1 + a_4 w^0}. \quad (13)$$

The parameters in (13) are shown as follows:

$$\begin{cases} a_0 = T_s^3\left(K_{p1}+K_{p2}\right) \\ a_1 = 2T_s^2(L_{xi}+L_{xg}) - T_s^3\left(K_{p1}+K_{p2}\right) \\ a_2 = 2T_s^2(L_{xi}+L_{xg}) + 4T_s C_x L_{xg} K_{p1} \\ a_3 = 8C_x L_{xi} L_{xg} - 4T_s C_x L_{xg} K_{p1} \\ a_4 = 8C_x L_{xi} L_{xg} \end{cases}. \quad (14)$$

$$G_{\rm close}(s) = \frac{\left(K_{p1}+K_{p2}\right)e^{-sT_s}}{s^3 L_{xi} L_{xg} C_x + s^2 L_{xg} C_x K_{p1} e^{-sT_s} + s(L_{xi}+L_{xg}) + \left(K_{p1}+K_{p2}\right)e^{-sT_s}}. \quad (12)$$

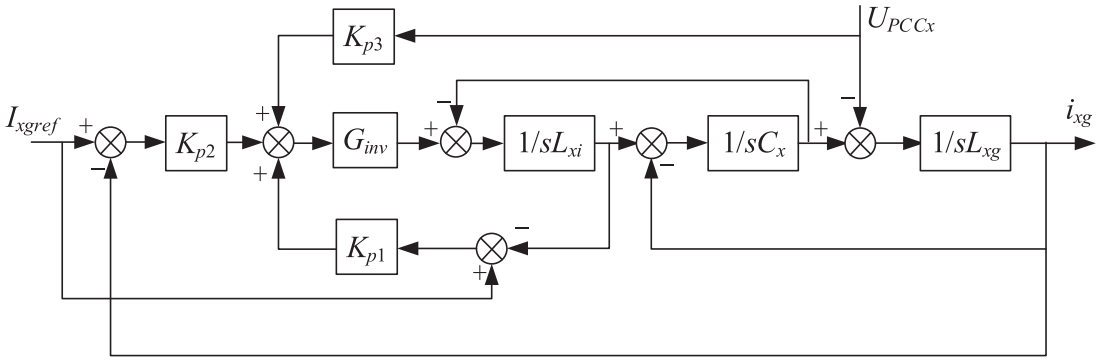

Fig. 3. Current control block diagram in s-domain.

To verify the adaptability of the D-D-Σ digital control proposed in this article to the wide range variation of grid impedance by *RC*, the value range of K_{p1} and K_{p2} can be obtained, which is shown in the following equation (see Appendix for a detailed Routh criterion process):

$$0 < K_{p1} + K_{p2} < \frac{2(L_{xi} + L_{xg})}{T_s}. \tag{15}$$

According to the definitions of K_{p1} and K_{p2} in the previous section, K_{p1}+K_{p2} always satisfies (15). This means that no matter how the grid impedance changes in the weak grid, K_{p1} and K_{p2} can meet the stability requirements. This proves that the proposed D-D-Σ digital control has strong adaptability to a weak grid.

IV. Online Identification of Grid Impedance

In the field of motor control, EKF is often used for parameter identification [41]. Similarly, it is also applied to grid impedance estimation [42]. In this article, a convenient extended Kalman filter method is proposed to identify the grid impedance. This method can reduce the input channels of state variables, which only need the grid-connected current. The generic state-space model for a linear system in the discrete-time domain is presented by

$$\begin{cases} \underline{x}_{k+1} = A_k \underline{x}_k + B_k \underline{u}_k + v_k \\ \underline{y}_k = H_k \underline{x}_k + w_k \end{cases} \tag{16}$$

where $\underline{x}_k$ is the state variables at the *k*th moment, *u* is the input vector, *A* is the state transition matrix, *B* is the input matrix, $\underline{y}$ is the output vector, *H* is the output matrix, and *v* and *w* are the system noise and measurement noise, respectively.

A parameter vector is added to the system state vector, which results in a nonlinear system description of the linear system with time-variant parameters. The physical measurement model remains unaffected [42]

$$\begin{cases} \begin{bmatrix} \underline{x}_{k+1} \\ \underline{\theta}_{k+1} \end{bmatrix} = f(\underline{x}_k, \underline{u}_k, \underline{\theta}_k) + \begin{bmatrix} v_{xk} \\ v_{\theta k} \end{bmatrix} \\ \underline{y}_k = \begin{bmatrix} C_d & 0 \\ 0 & 0 \end{bmatrix} \begin{bmatrix} \underline{x}_k \\ \underline{\theta}_k \end{bmatrix} + \begin{bmatrix} w_k \\ 0 \end{bmatrix} \end{cases} \tag{17}$$

The grid-connected currents i_{xg} and the voltages $U_{\mathrm{PCC}x}$ at the PCC are sampled for gird impedance estimation. In the D-D-Σ digital control method, the currents of L_{xi} and L_{xg} are considered to be consistent because the currents can be tracked accurately. Therefore, an *LCL* filter can be equivalent to an *L* filter in inductance identification. Set the identified impedance to ΔL_g. ΔR_g is the equivalent resistance. Among them, ΔL_g includes the inverter-side impedance, grid-side impedance, and impedance variation. The fluctuation of grid-side impedance can be regarded as the fluctuation of grid impedance. According to the circuit shown in Fig. 1, the α-axis and β-axis grid-connected currents are selected as the state vectors, and the state-space equation is written as follows:

$$\begin{aligned} \frac{d}{dt}\begin{bmatrix} i_{g\alpha} \\ i_{g\beta} \end{bmatrix} &= \begin{bmatrix} -\frac{\Delta R_g}{\Delta L_g} & 0 \\ 0 & \frac{\Delta R_g}{\Delta L_g} \end{bmatrix} \begin{bmatrix} i_{g\alpha} \\ i_{g\beta} \end{bmatrix} \\ &\quad + \begin{bmatrix} \frac{1}{\Delta L_g} & 0 \\ 0 & \frac{1}{\Delta L_g} \end{bmatrix} \begin{bmatrix} u_{\alpha o} - e_\alpha \\ u_{\beta o} - e_\beta \end{bmatrix} \end{aligned} \tag{18}$$

where $i_{g\alpha}$, $u_{\alpha o}$, and e_α are the components of i_{xg}, u_{xo}, and e_x in the α-axis, respectively. $i_{g\beta}$, $u_{\beta o}$, and e_β are the components in the β-axis, respectively.

Generally, the grid voltage e_x is considered an ideal three-phase sinusoidal power supply. Therefore, the voltage signal e_x of the ideal power grid can be constructed according to the phase information, which is obtained by PLL. Thus, the input sampling variables of EKF can be reduced. Meanwhile, the fundamental component of the inverter output voltage u_{xo} can be obtained by multiplying the dc-side voltage and the duty cycle d_x as

$$u_{xo} = \frac{U_{\mathrm{dc}}}{2} d_x \tag{19}$$

where $U_{\mathrm{dc}}/2$ is the dc-side voltage because a T-type three-level inverter is finally used as the research object in this article.

By discretizing (18), the state-space equation in the discrete-time domain can be obtained as (20) shown at the bottom of the next page. As a result, the Jacobian matrix of EKF can be expressed by (21) shown at the bottom of the next page. To introduce the process of EKF estimating grid impedance in more detail, the flowchart of EKF implementation is shown in Fig. 4, where $\underline{y} = (i_{g\alpha}, i_{g\beta})^T$ is the grid-connected current measured in real time, $\tilde{P}_k$ is the error covariance matrix of state variables in prediction process at the *k*th moment, *K* is the Kalman filter gain matrix, *Q* is the system noise covariance matrix, *R*

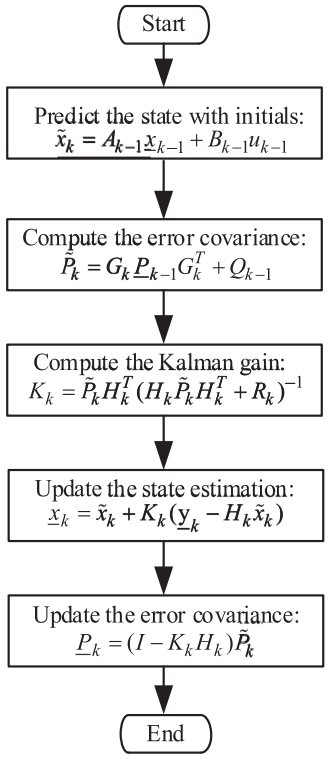

Fig. 4. Flowchart of EKF implementation.

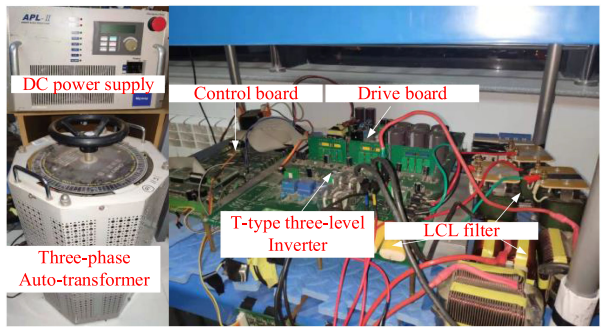

Fig. 5. Experimental platform of a T-type three-level inverter with an *LCL* filter.

is the measurement noise covariance matrix. In practice, the noise covariance matrices are assumed to be constant diagonal matrices.

As mentioned above, K_{p2} affects the current tracking accuracy and K_{p1} affects the resonance suppression effect. With the variation of filter inductance, the resonant frequency also changes. However, the change of grid impedance is equivalent to the change of grid-side inductance. According to (11), the change of L_{xg} will bring about the change of K_{p2} but cannot improve the resonance suppression effect, which is not allowed. Therefore, a gain correction method is proposed to deal with the variation of inductance.

It can be seen from (15) that $K_{p1}+K_{p2}$ calculated by (11) meets the requirement of stability. Whether the inverter-side impedance or the grid impedance changes, the following equation represents the relationship of $K_{p1}+K_{p2}$:

$$K_{p1}+K_{p2}=\frac{2\left(L_{xi}+\Delta L_{xi}+L_{xg}+\Delta L_{xg}\right)}{U_{\mathrm{dc}}T_s}=\frac{2\Delta L_g}{U_{\mathrm{dc}}T_s} \tag{22}$$

where ΔL_{xg} represents the variation of grid impedance and ΔL_{xi} represents the variation of inverter-side impedance.

$$\begin{cases} \underbrace{\begin{bmatrix} i_{g\alpha}(k+1) \\ i_{g\beta}(k+1) \\ \Delta R_g(k+1) \\ \Delta L_g(k+1) \end{bmatrix}}_{\underline{x}_{k+1}} = \underbrace{\begin{bmatrix} 1-\dfrac{T_s\Delta R_g}{\Delta L_g} & 0 & 0 & 0 \\ 0 & 1-\dfrac{T_s\Delta R_g}{\Delta L_g} & 0 & 0 \\ 0 & 0 & 0 & 0 \\ 0 & 0 & 0 & 0 \end{bmatrix}}_{A_k} \underbrace{\begin{bmatrix} i_{g\alpha}(k) \\ i_{g\beta}(k) \\ \Delta R_g(k) \\ \Delta L_g(k) \end{bmatrix}}_{\underline{x}_k} + \underbrace{\begin{bmatrix} \dfrac{\Delta R_g}{\Delta L_g} & 0 \\ 0 & \dfrac{\Delta R_g}{\Delta L_g} \\ 0 & 0 \\ 0 & 0 \end{bmatrix}}_{B_k} \underbrace{\begin{bmatrix} u_{\alpha o}(k)-e_\alpha(k) \\ u_{\beta o}(k)-e_\beta(k) \end{bmatrix}}_{\underline{u}_k} \\ \underbrace{\begin{bmatrix} i_{g\alpha}(k) \\ i_{g\beta}(k) \end{bmatrix}}_{\underline{y}_k} = \underbrace{\begin{bmatrix} 1 & 0 & 0 & 0 \\ 0 & 1 & 0 & 0 \end{bmatrix}}_{H_k} \underbrace{\begin{bmatrix} i_{g\alpha}(k) \\ i_{g\beta}(k) \\ \Delta R_g(k) \\ \Delta L_g(k) \end{bmatrix}}_{\underline{x}_k} \end{cases} \tag{20}$$

$$\begin{cases} G_k = \begin{bmatrix} 1-\dfrac{T_s\Delta R_g}{\Delta L_g} & 0 & -\dfrac{T_s}{\Delta L_g}i_{2\alpha}(k) & \dfrac{T_s\Delta R_g i_{2\alpha}(k)}{\Delta L_g^2}-\dfrac{T_s\left[u_{\alpha o}(k)-e_\alpha(k)\right]}{\Delta L_g^2} \\ 0 & 1-\dfrac{T_s\Delta R_g}{\Delta L_g} & -\dfrac{T_s}{\Delta L_g}i_{2\beta}(k) & \dfrac{T_s\Delta R_g i_{2\beta}(k)}{\Delta L_g^2}-\dfrac{T_s\left[u_{\beta o}(k)-e_\beta(k)\right]}{\Delta L_g^2} \\ 0 & 0 & 1 & 0 \\ 0 & 0 & 0 & 1 \end{bmatrix}. \\ H_k = \begin{bmatrix} 1 & 0 & 0 & 0 \\ 0 & 1 & 0 & 0 \end{bmatrix} \end{cases} \tag{21}$$

TABLE I
EXPERIMENTAL PARAMETERS

Parameter	Value
DC-link voltage	200 V
Grid voltage(pk-pk)	100 V
Grid-connected current	10 A
Rated power of inverter	1 kW
Inverter-side inductor L_{xi}	3.8 mH
Grid-side inductor L_{xg}	1.1 mH
Filter capacitor C_f	20 μF
Fundamental frequency	50 Hz
Switching frequency	10 kHz
Sampling frequency	10 kHz

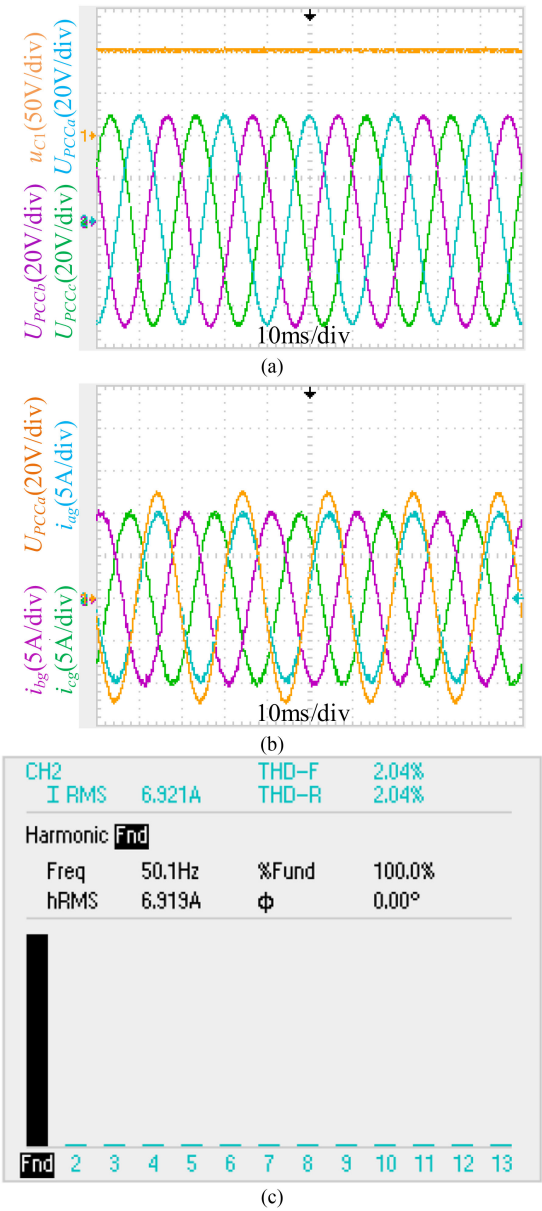

Fig. 6. Control effect of D-D-Σ digital control under a balanced grid. (a) Capacitance voltage u_{C1} on dc-side and three-phase voltages at PCC. (b) Three-phase grid-connected currents. (c) THD of phase a current.

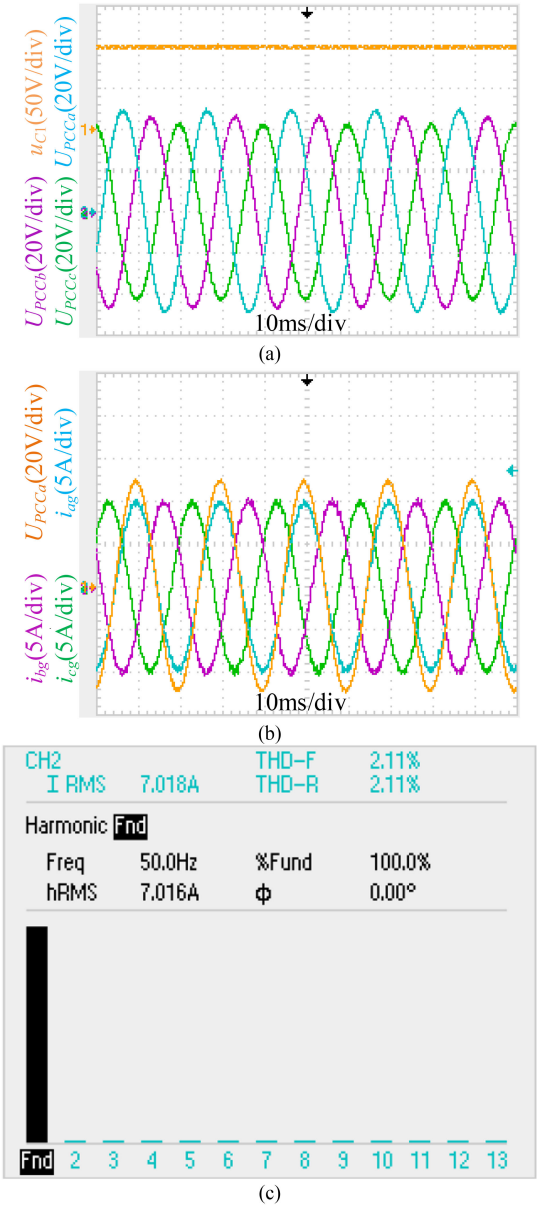

Fig. 7. Control effect of D-D-Σ digital control under an unbalanced grid. (a) Capacitance voltage u_{C1} on dc-side and three-phase voltages at PCC. (b) Three-phase grid-connected currents. (c) THD of phase a current.

Therefore, keeping K_{p2} unchanged, the corrected K_{p1} can be expressed as

$$K_{p1}^{'} = \frac{2\left(\Delta L_g - L_{xg}\right)}{U_{\mathrm{dc}} T_s}. \tag{23}$$

The corrected K_{p1} and K_{p2} cannot only ensure the current tracking accuracy but also ensure the resonance suppression under the variation of impedance.

V. EXPERIMENTAL VERIFICATION

To verify the strong adaptability control based on the D-D-Σ digital control proposed in this article, an experimental prototype with a T-type three-level inverter and an *LCL* filter is

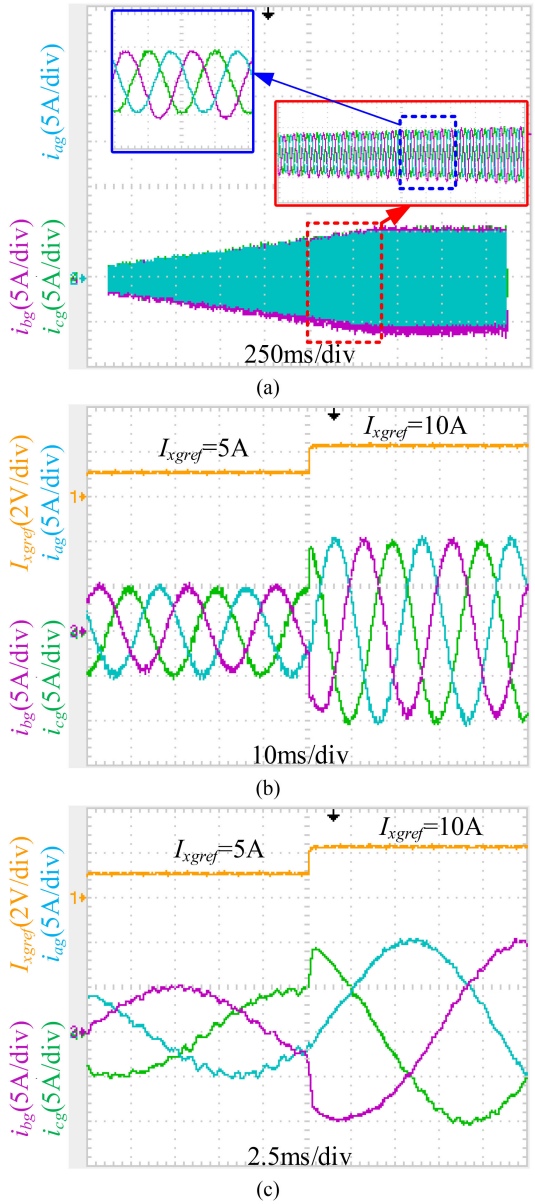

Fig. 8. Startup performance. (a) Soft start. (b) Current mutation. (c) Partial diagram of current mutation.

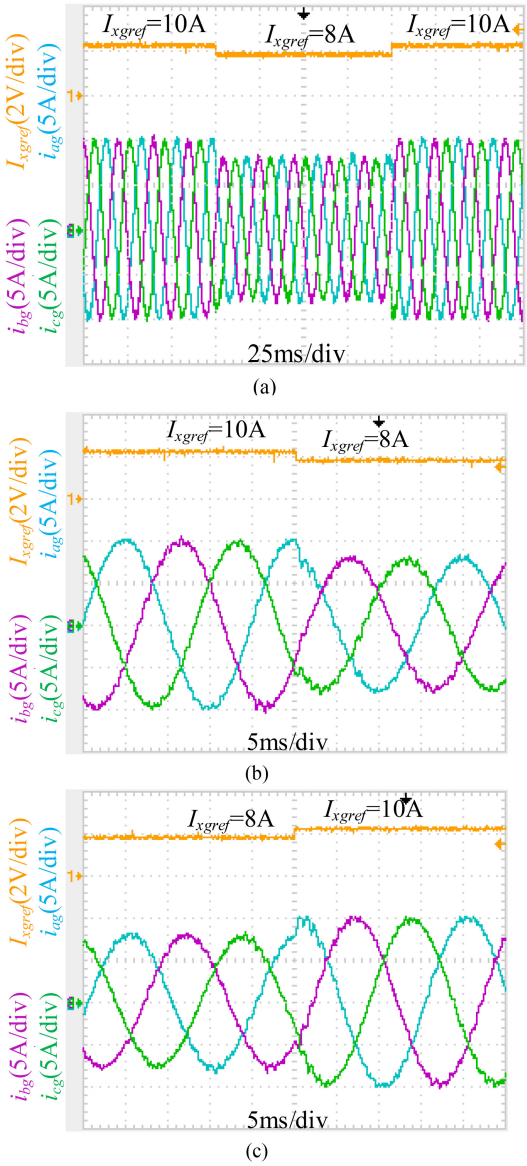

Fig. 9. Dynamic response capability. (a) Overall dynamic waveform. (b) Reducing grid-connected currents. (c) Increasing grid-connected currents.

built. Fig. 5 shows the experimental platform. The controller is composed of STM32F407+EPM240T100C5N. In this article, a zero-sequence injection method is used to control the neutral-point potential [43]. Table I shows the experimental parameters.

A. Control Effect With D-D-Σ Digital Control Under Different Grid Conditions

Fig. 6 shows the grid-connected current waveforms under balanced grid conditions. The voltages at PCC are shown in Fig. 6(a). The grid-connected currents are shown in Fig. 6(b). In Fig. 6(a), the upper capacitive voltage on the dc side is 100 V, which proves that the neutral-point potential is balanced. It can be seen from Fig. 6(b) that the grid-connected currents are sinusoidal and symmetrical, verifying the feasibility of the designed inverter with D-D-Σ digital control. THD in Fig. 6(c) is less than 3%, meeting the grid-connected requirements. Meanwhile, the grid-connected current and the corresponding grid voltage are in phase. Moreover, the inverter is also tested with the unbalanced grid. As shown in Fig. 7, even if the voltages at PCC are unbalanced, the grid-connected currents can still be sinusoidal and symmetrical, which meets the requirements of grid connection. This proves that the inverter with D-D-Σ digital control has good grid-connected performance.

B. Dynamic Response Capability With D-D-Σ Digital Control

Fig. 8 shows the startup performance of grid-connected current control based on D-D-Σ method. This starting performance adopts a soft start mode to make the current change slowly from 0 to 5 A. Meanwhile, the current variation process from 5 to 10 A adopts the mode of current mutation, as shown in Fig. 8(b) and

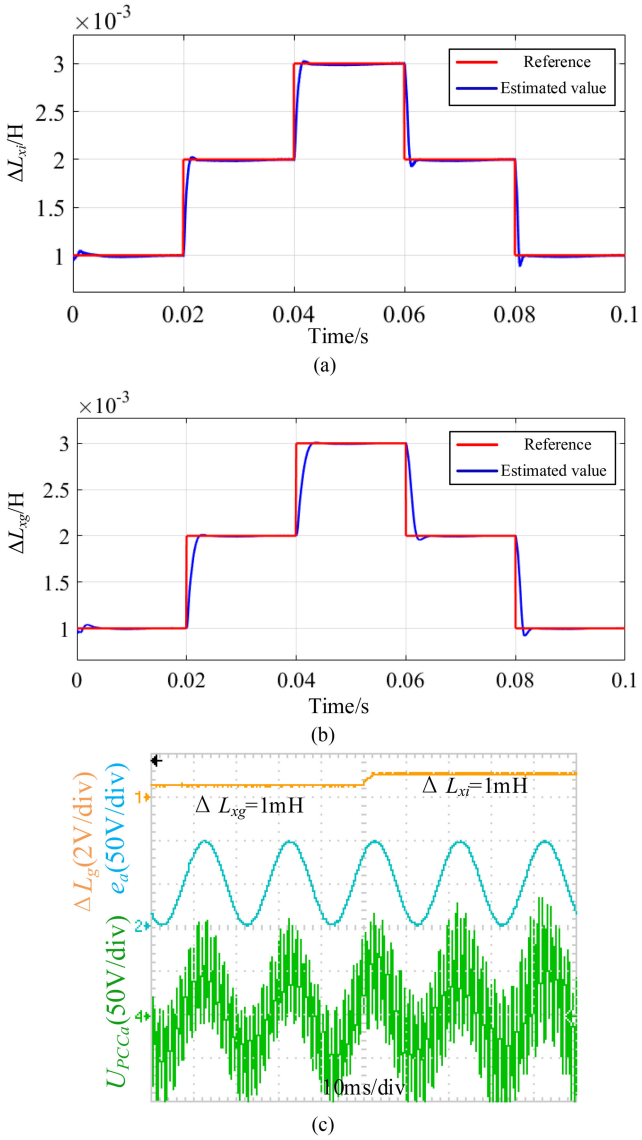

Fig. 10. Waveforms of voltage fluctuation and grid impedance estimation by EKF. (a) Simulation waveform of variation of L_{xi}. (b) Simulation waveform of variation of L_{xg}. (c) Experimental waveform.

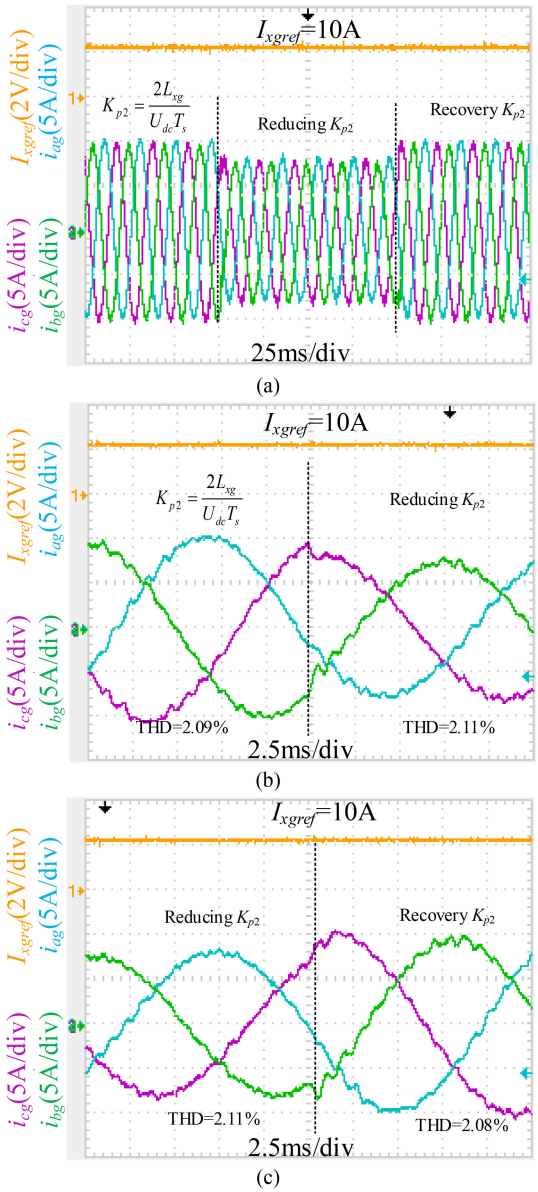

Fig. 11. Control effect of different K_{p2}. (a) Overall dynamic waveform. (b) Reducing K_{p2}. (c) Increasing K_{p2}.

(c). The processing time of the current mutation is short, i.e., only 1.5 ms.

For the dynamic response capability test, Fig. 9 shows the transient response of grid-connected currents changing from 10 to 8 A and from 8 back to 10 A. It is shown that the transient response time from 8 to 10 A is about 1.25 ms, as shown in Fig. 9(b). For the transient from 10 to 8 A, the grid-connected currents reach their steady state at the same time, and the response time is about 1 ms, as shown in Fig. 9(c). Fig. 9 shows that the proposed D-D-Σ digital control has a strong rapidity for the current dynamic response.

C. Verification of EKF

Fig. 10 shows the simulation and experimental results of the parameter identification method. Since the actual grid impedance value is not known, the EKF method is verified in the simulation. The simulation waveforms as shown in Fig. 10(a) and (b) are obtained by changing L_{xi} and L_{xg}, respectively. It can be seen from the simulation waveforms that the proposed method can accurately identify the inductance parameters no matter which inductance value of the *LCL* filter changes.

In the experiment, the author connects an inductor between the PCC and the power grid to simulate the grid impedance. The variation of this inductor is equivalent to the variation of grid impedance. As shown in Fig. 10(c), the grid impedance values ΔL_g are identified by the EKF method when L_{xi} and L_{xg}, change, respectively. Channel 2 of the oscilloscope is the ideal grid voltage waveform of phase a, which gets good sinusoidal characteristics. Channel 4 shows the voltage of phase a at PCC. Channel 1 in Fig. 10 is the grid impedance value ΔL_g estimated

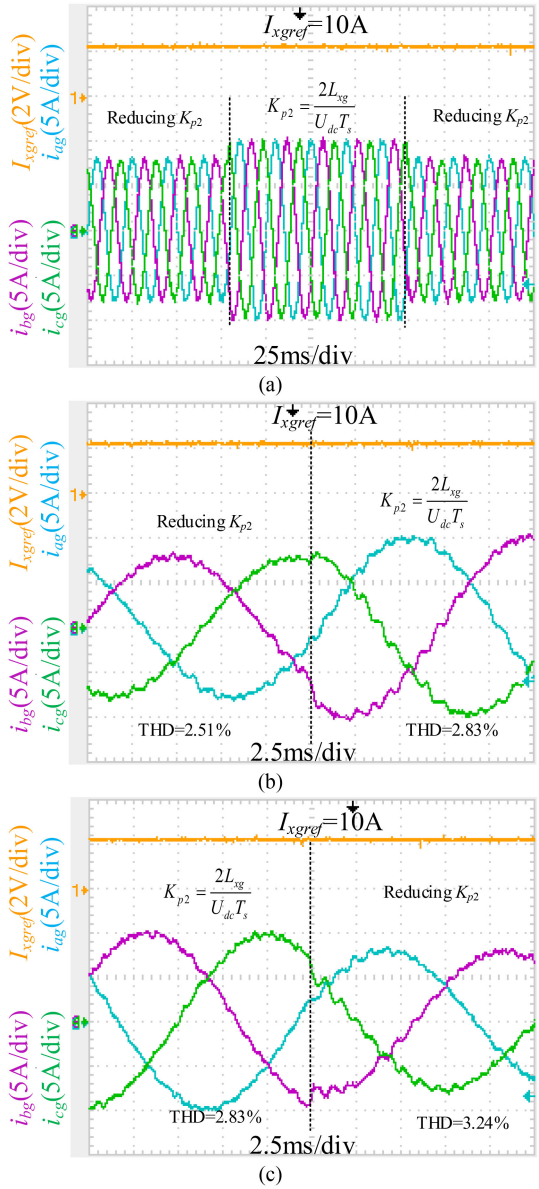

Fig. 12. Control effect of different K_{p2}. (a) Overall dynamic waveform. (b) Increasing K_{p2}. (c) Reducing K_{p2}.

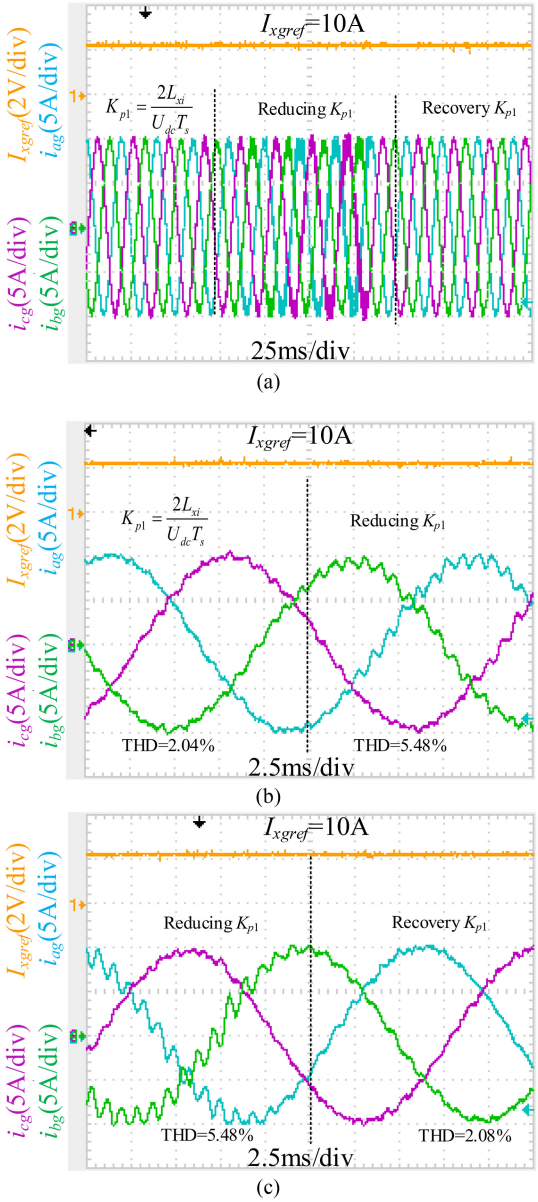

Fig. 13. Control effect of different K_{p1}. (a) Overall dynamic waveform. (b) Reducing K_{p1}. (c) Increasing K_{p1}.

by EKF. The waveform of L_g is observed through the digital-to-analog conversion function of the controller. The inverter-side inductance L_{xi} and grid impedance L_{xg} are changed by 1 mH, respectively. It is seen from Fig. 10 that the validity of the EKF proposed in this article is proved, which only needs the voltage at the PCC and grid-connected current. The proposed EKF with fewer inputs can accurately identify the grid impedance.

D. Control Effect With D-D-Σ Digital Control Under Different K_{p1} *and* K_{p2}

As the meaning of K_{p1} and K_{p2} are mentioned earlier, here, the value of K_{p1} and K_{p2} are changed to verify the correctness of this statement. In Fig. 11(a), the value of K_{p2} in (11) is used, and then the value of K_{p2} is reduced, and finally, it is restored. When K_{p2} is reduced as shown in Fig. 11(b), the amplitude of grid-connected currents is reduced. When K_{p2} is restored as shown in Fig. 11(c), the grid-connected currents can accurately track the reference value of 10 A. The dynamic process opposite to that in Fig. 11 is reflected in Fig. 12. When the value of K_{p2} is less than the value in (11), the amplitude of grid-connected currents cannot reach the reference value. When K_{p2} in (11) is used, the grid-connected currents can accurately track the reference value. This proves that K_{p2} affects the tracking accuracy of the grid-connected currents. The current fluctuations in Fig. 11(b) and (c) are due to the distortion of the oscilloscope when the time axis is expanded from 25 to 2.5 ms/div.

Similarly, a similar conclusion that K_{p1} affects resonance suppression effect can be obtained from Figs. 13 and 14. In

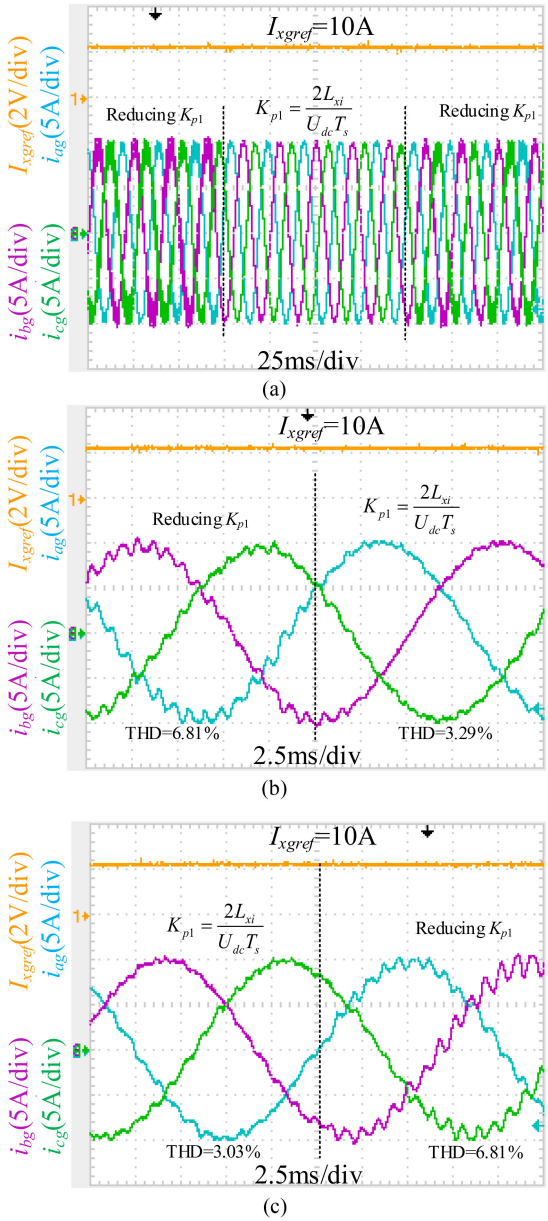

Fig. 14. Control effect of different K_{p1}. (a) Overall dynamic waveform. (b) Increasing K_{p1}. (c) Reducing K_{p1}.

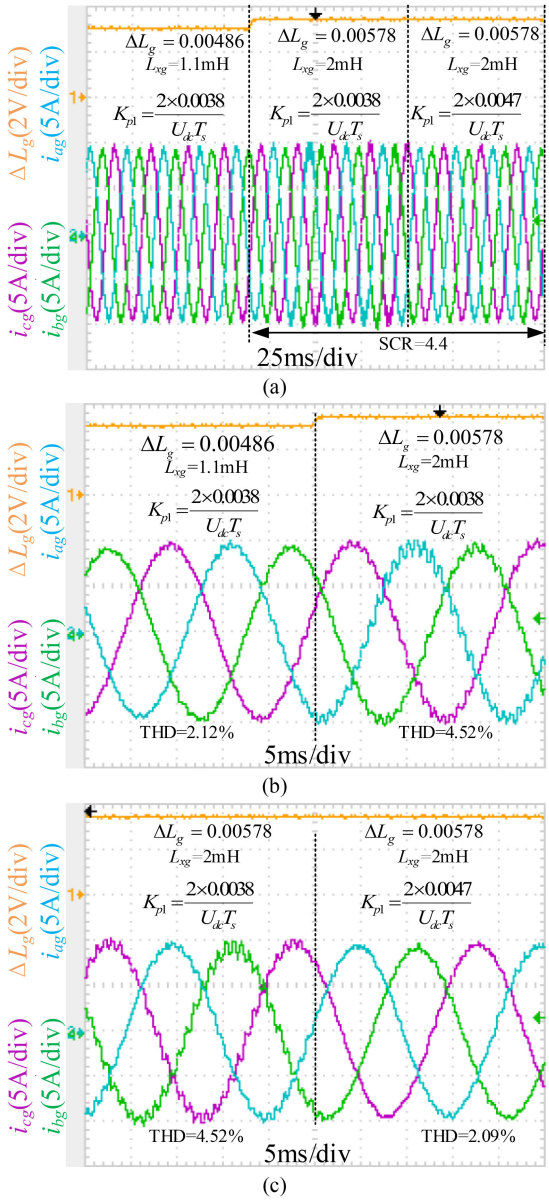

Fig. 15. Control effect of different L_{xg} under D-D-Σ digital control. (a) Overall dynamic waveform. (b) Increase L_{xg} and fixed K_{p1}. (c) Increase K_{p1} and fixed L_{xg}.

Fig. 13(b), the current fluctuation is larger than that before reducing K_{p1}. This kind of fluctuation is not caused by the change in the time axis. It can be seen from Fig. 13(a) that the current fluctuation is caused when the value of K_{p1} is reduced, which reduces the resonance suppression effect. The process in Fig. 13 is opposite to that in Fig. 14, which also proves that K_{p1} described in this article affects the resonance suppression effect.

E. Control Effect With D-D-Σ Digital Control Under Different L_{xi} *and* L_{xg}

To verify the adaptability of the D-D-Σ digital control proposed in this article when the inductance changes, the inverter is tested under different filter inductances L_{xg}. Fig. 15 shows the grid-connected currents waveform when the grid-side inductance changes. The equivalent grid impedance after the inductance on the grid-side changes is 0.9 mH, and the corresponding short circuit ratio is 4:4. The estimated inductance ΔL_g based on the EKF method is marked in the figures. When the inductance of the grid-side increases and K_{p1} remains unchanged, the resonance frequency decreases, and the fixed K_{p1} does not fully meet the resonance suppression requirements. Therefore, in Fig. 15(b), the harmonics appear in the grid-connected currents. When K_{p1} is amended, it can be seen from Fig. 15(c) that the resonance is completely suppressed to meet the requirements of grid connection. This proves that the proposed D-D-Σ digital control has strong adaptability to the variation of grid inductance. Of course, when the inductance on the inverter-side

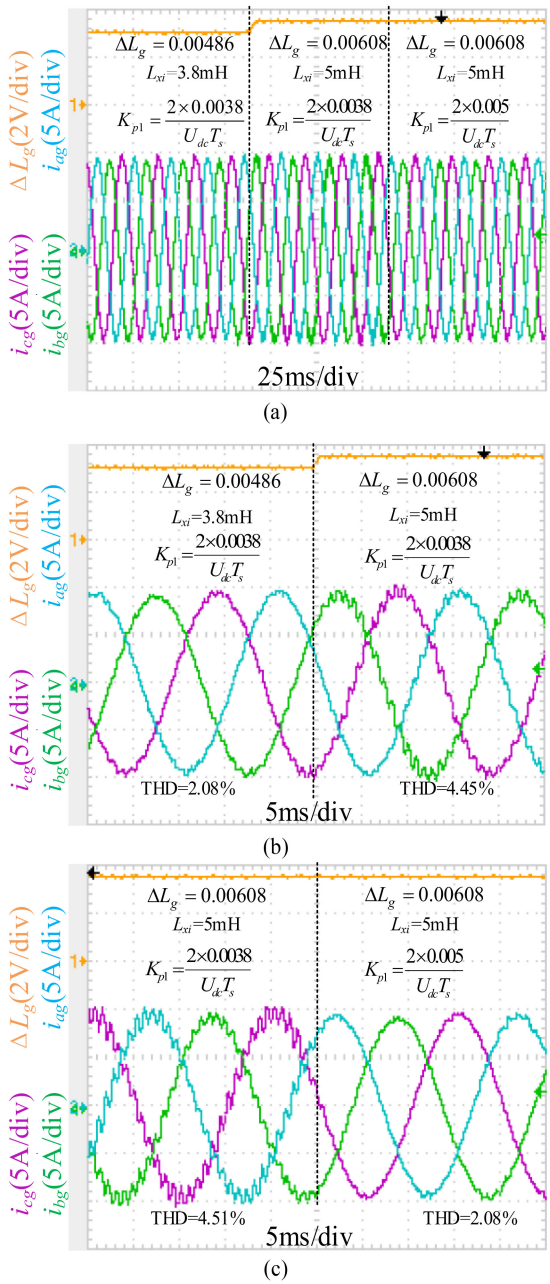

Fig. 16. Control effect of different L_{xi} under D-D-Σ digital control. (a) Overall dynamic waveform. (b) Increase L_{xi} and fixed K_{p1}. (c) Increasing L_{xi} and K_{p1}.

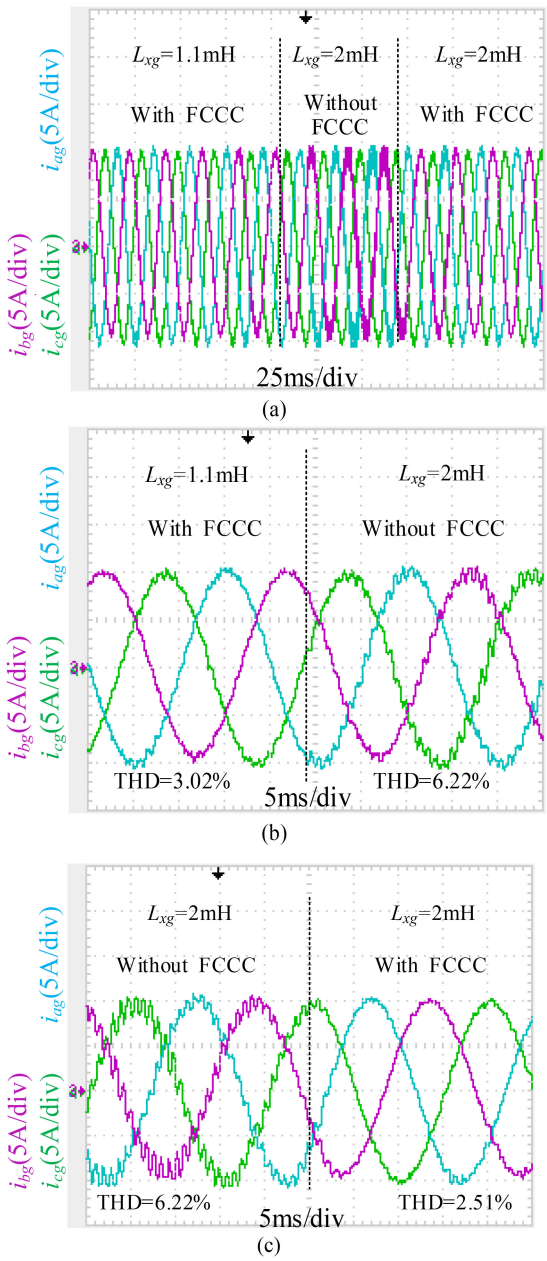

Fig. 17. Control effect of different L_{xg} under D-Σ digital control with FCCC. (a) Overall dynamic waveform. (b) Switching from with FCCC to without FCCC. (c) Switching from without FCCC to with FCCC.

changes, Fig. 16 shows that the value of K_{p1} in (11) can still ensure the safe and stable operation of the inverter.

Moreover, to show the advantages of D-D-Σ digital control, it is compared with the method in reference [20]. The D-D-Σ digital control method is switched to the D-Σ method with FCCC under the same working conditions, and the results are shown in Figs. 17 and 18. From the comparison results, it can be seen that when the inductance changes dynamically or increases the resonance suppression effect, the proposed D-D-Σ digital control method has good rapidity, which saves the calculation time of filter- capacitor current. Table II shows the performance comparison of the two control methods. The D-Σ control method is applied to an single-phase *LCL*-type inverter. In this article, it is extended to the three-phase grid-connected inverter. When the sampled quantities are the same, the control method proposed in this article is simpler and less computational. Meanwhile, this article not only considers the grid impedance under the weak grid but also considers the influence of the variation of filter inductance.

F. Phase Control of Grid-Connected Current Based on D-D-Σ Control

Fig. 19 shows grid-connected current switching waveforms at different phase angles *pf*. In this article, three groups of switching

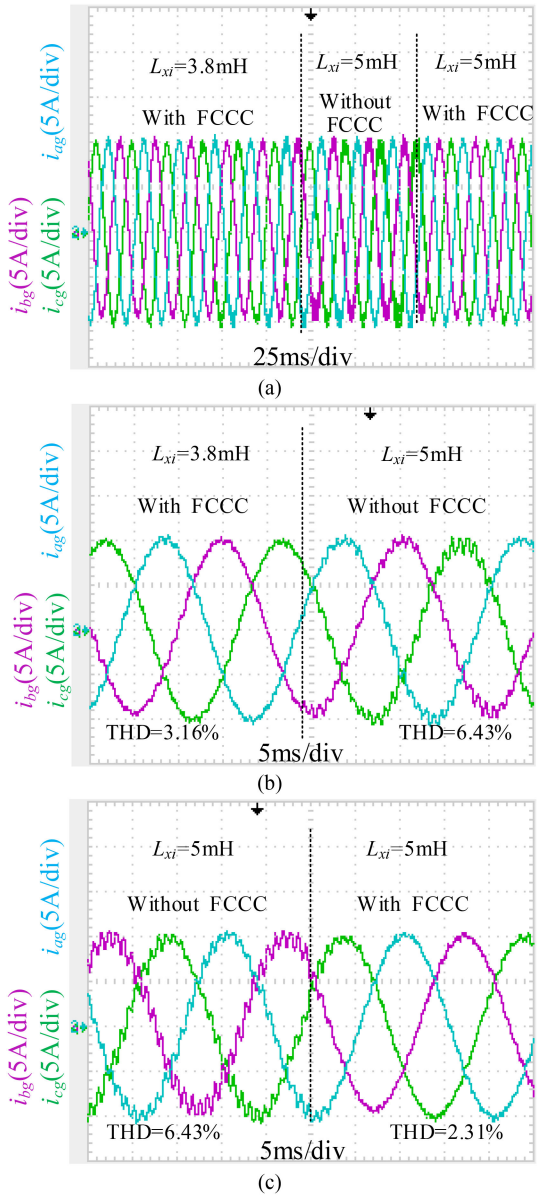

Fig. 18. Control effect of different L_{xi} under D-Σ digital control with FCCC. (a) Overall dynamic waveform. (b) Switching from with FCCC to without FCCC. (c) Switching from without FCCC to with FCCC.

experiments are carried out, which are the switching between $pf>0$ and $pf=0$, $pf<0$ and $pf=0$, and $pf>0$ and $pf<0$. It can be seen from the experimental waveforms that the grid-connected current control method based on D-D-Σ control proposed in this article can quickly and accurately realize current tracking under different phase angles of grid-connected current reference values.

G. Control Performance Under Multiple Disturbances

Fig. 20 shows the grid-connected current change waveforms when the $I_{xg\mathrm{ref}}$ and L_{xg} change at the same time. In Fig. 20(a), when the $I_{xg\mathrm{ref}}$ and L_{xg} change at the same time, the harmonic of grid-connected current occurs because of unchanged control parameters. The resonance effect is not completely suppressed.

TABLE II
PERFORMANCE COMPARISION OF TWO CONTROL METHODS

	D-Σ-Σ	D-Σ with FCCC
Application object	Three-phase inverter	Single-phase bidirectional inverter
Number of sampled quantities	3	3
Controller complexity	Easy	Complex
Calculation quantity	Less	Large
Inductance estimation method	Yes	No
Change of filter inductance	Considered	Unconsidered

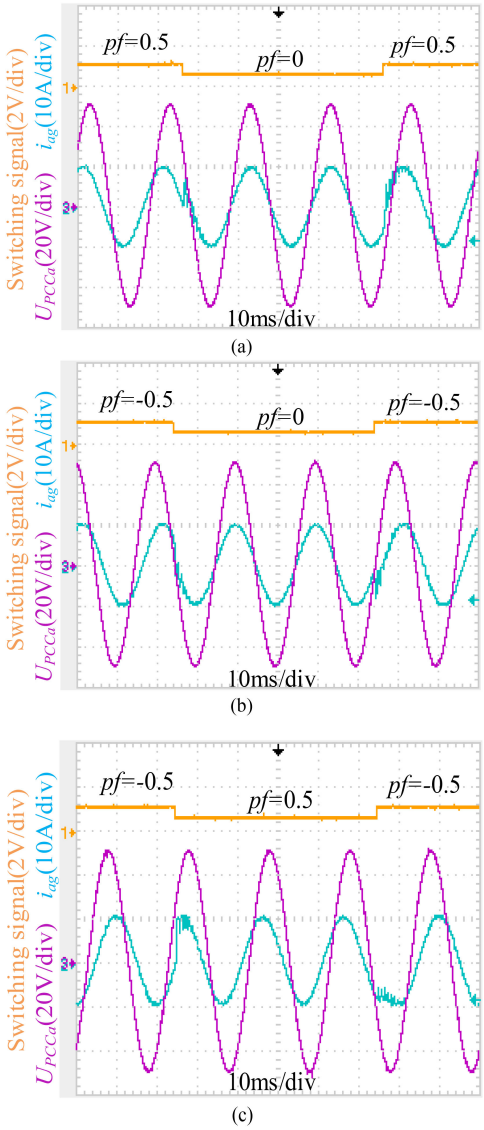

Fig. 19. Switching waveforms of grid-connected current under different phase angles pf based on D-D-Σ control. (a) Switching waveform between $pf=0.5$ and $pf=0$. (b) Switching waveform between $pf=-0.5$ and $pf=0$. (c) Switching waveform between $pf=-0.5$ and $pf=0.5$.

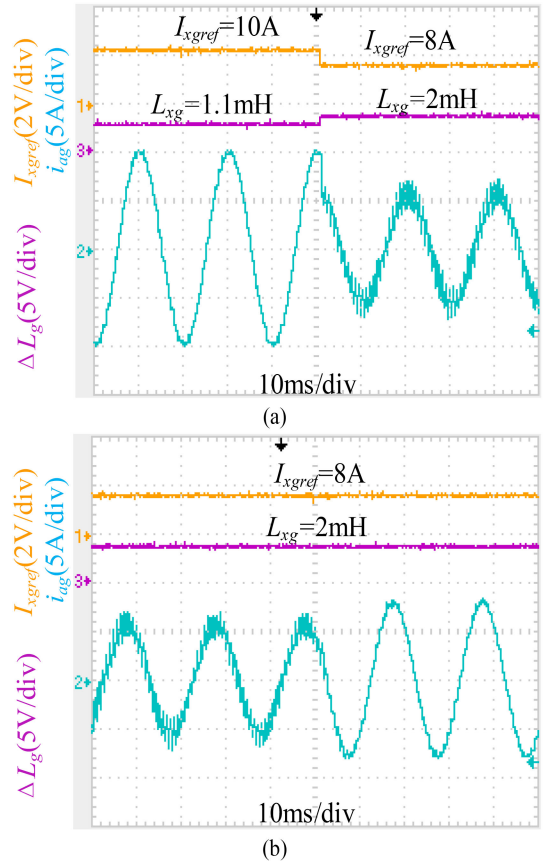

Fig. 20. Switching waveforms of grid-connected current under different $I_{xg\mathrm{ref}}$ and L_{xg} based on D-D-Σ control. (a) Multiple disturbances occur when the control parameters remain unchanged. (b) Multiple disturbances occur when the control parameters changed.

Meanwhile, the grid-connected current tracking effect is poor because K_{p2} remains unchanged. In Fig. 20(b), when the control parameters are modified according to the method proposed in this article, it can be found that the resonance effect of the grid-connected current is completely suppressed. The grid-connected current amplitude can accurately track the reference value 8 A.

VI. Conclusion

In this article, a D-D-Σ digital control suitable for the *LCL* -type grid-connected inverter is proposed, which can take both grid current tracking and resonance suppression into account. Different from the traditional D-Σ digital control, the proposed D-Σ digital control is used for two inductances of the *LCL* filter simultaneously. The proposed D-D-Σ digital control does not need coordinate transformation and is more suitable for unbalanced grid conditions. Meanwhile, a full inductance parameter identification method based on EKF proposed in this article is used to deal with variations of filter inductance and grid impedance. The strong adaptability of D-D-Σ digital control to a wide range of variations of inductance is demonstrated quantitatively by a gain correction method. It is proved by experiments that the proposed D-D-Σ digital control can ensure that the grid-connected current of the inverter is sinusoidal and symmetrical under balanced or unbalanced grids. For the wide variation of inductance, the proposed D-D-Σ digital control and gain correction method can ensure a stable inverter.

TABLE III
Discrete Routh Array in *W*-Domain

Sequence	Coefficient Value		
w^4	a_0	a_2	a_4
w^3	a_1	a_3	
w^2	$\frac{a_1a_2-a_0a_3}{a_1}$	a_4	
w^1	$\frac{(a_1a_2-a_0a_3)a_3-a_1a_1a_4}{a_1a_2-a_0a_3}$		
w^0	a_4		

Appendix

The characteristic equation in *w*-domain can be obtained as

$$a_0w^4+a_1w^3+a_2w^2+a_3w^1+a_4w^0=0. \tag{A-1}$$

The discrete Routh array in *w*-domain can be constructed as in Table III.

The stability of the system depends on positive or negative coefficients of the first column of the discrete Routh array. In a stable system, the first column coefficients of the discrete Routh array can be obtained as

$$\begin{cases} a_0>0 \\ a_1>0 \\ a_1a_2-a_0a_3>0 \\ (a_1a_2-a_0a_3)\,a_3-a_1a_1a_4>0 \\ a_4>0 \end{cases}. \tag{A-2}$$

References

[1] L. Zhou et al., "Inverter-current-feedback resonance-suppression method for LCL-type DG system to reduce resonance-frequency offset and grid-inductance effect," *IEEE Trans. Ind. Electron.*, vol. 65, no. 9, pp. 7036–7048, Sep. 2018.

[2] B. Liu, Q. Wei, C. Zou, and S. Duan, "Stability analysis of LCL-type grid-connected inverter under single-loop inverter-side current control with capacitor voltage feedforward," *IEEE Trans. Ind. Inform.*, vol. 14, no. 2, pp. 691–702, Feb. 2018.

[3] R. Guzman, L. G. de Vicuña, M. Castilla, J. Miret, and J. de la Hoz, "Variable structure control for three-phase LCL-filtered inverters using a reduced converter model," *IEEE Trans. Ind. Electron.*, vol. 65, no. 1, pp. 5–15, Jan. 2018.

[4] M. Reyes, P. Rodriguez, S. Vazquez, A. Luna, R. Teodorescu, and J. M. Carrasco, "Enhanced decoupled double synchronous reference frame current controller for unbalanced grid-voltage conditions," *IEEE Trans. Power Electron.*, vol. 27, no. 9, pp. 3934–3943, Sep. 2012.

[5] G. H. Bode, P. Chiang Loh, M. J. Newman, and D. G. Holmes, "An improved robust predictive current regulation algorithm," *IEEE Trans. Ind. Appl.*, vol. 41, no. 6, pp. 1720–1733, Nov./Dec. 2005.

[6] D. N. Zmood and D. G. Holmes, "Stationary frame current regulation of PWM inverters with zero steady-state error," *IEEE Trans. Power Electron.*, vol. 18, no. 3, pp. 814–822, May 2003.

[7] J. Xia, Y. Guo, X. Zhang, J. Jatskevich, and N. Amiri, "Robust control strategy design for single-phase grid-connected converters under system perturbations," *IEEE Trans. Ind. Electron.*, vol. 66, no. 11, pp. 8892–8901, Nov. 2019.

[8] C. Xia, M. Wang, Z. Song, and T. Liu, "Robust model predictive current control of three-phase voltage source PWM rectifier with online disturbance observation," *IEEE Trans. Ind. Inform.*, vol. 8, no. 3, pp. 459–471, Aug. 2012.

[9] C. S. Lim, H. H. Goh, and S. S. Lee, "Long-prediction-horizon near-optimal model predictive grid current control for PWM-driven VSIs with LCL filters," *IEEE Trans. Power Electron.*, vol. 36, no. 2, pp. 2246–2257, Feb. 2021.
[10] T. Jin, L. Li, and K. M. Smedley, "A universal vector controller for four-quadrant three-phase power converters," *IEEE Trans. Circuits Syst. I, Reg. Papers*, vol. 54, no. 2, pp. 377–390, Feb. 2007.
[11] K. Nishida, T. Ahmed, and M. Nakaoka, "Cost-effective deadbeat current control for wind-energy inverter application with LCL filter," *IEEE Trans. Ind. Appl.*, vol. 50, no. 2, pp. 1185–1197, Mar./Apr. 2014.
[12] Y. A.-R. I. Mohamed and E. F. El-Saadany, "An improved deadbeat current control scheme with a novel adaptive self-tuning load model for a three-phase PWM voltage-source inverter," *IEEE Trans. Ind. Electron.*, vol. 54, no. 2, pp. 747–759, Apr. 2007.
[13] J. Chen, X. Zhang, and C. Wen, "Harmonics attenuation and power factor correction of a more electric aircraft power grid using active power filter," *IEEE Trans. Ind. Electron.*, vol. 63, no. 12, pp. 7310–7319, Dec. 2016.
[14] F. Wu, X. Li, and J. Duan, "Improved elimination scheme of current zero-crossing distortion in unipolar hysteresis current controlled grid-connected inverter," *IEEE Trans. Ind. Inform.*, vol. 11, no. 5, pp. 1111–1118, Oct. 2015.
[15] Z. Song, W. Chen, and C. Xia, "Predictive direct power control for three-phase grid-connected converters without sector information and voltage vector selection," *IEEE Trans. Power Electron.*, vol. 29, no. 10, pp. 5518–5531, Oct. 2014.
[16] Y. Zhang and C. Qu, "Direct power control of a pulse width modulation rectifier using space vector modulation under unbalanced grid voltages," *IEEE Trans. Power Electron.*, vol. 30, no. 10, pp. 5892–5901, Oct. 2015.
[17] O. Kukrer, S. Bayhan, and H. Komurcugil, "Model-based current control strategy with virtual time constant for improved dynamic response of three-phase grid-connected VSI," *IEEE Trans. Ind. Electron.*, vol. 66, no. 6, pp. 4156–4165, Jun. 2019.
[18] Y. Han, Z. Li, P. Yang, C. Wang, L. Xu, and J. M. Guerrero, "Analysis and design of improved weighted average current control strategy for LCL-type grid-connected inverters," *IEEE Trans. Energy Convers.*, vol. 32, no. 3, pp. 941–952, Sep. 2017.
[19] T. Wu, C. Chang, L.-C. Lin, and H. Hsieh, "D-Σ digital control for a three-phase transformerless bi-directional inverter with wide inductance variation," in *Proc. IEEE ECCE Asia Downunder*, 2013, pp. 73–79.
[20] T. Wu, L. Lin, N. Yao, Y. Chen, and Y. Chang, "Extended application of D-Σ digital control to a single-phase bidirectional inverter with an LCL filter," *IEEE Trans. Power Electron.*, vol. 30, no. 7, pp. 3903–3911, Jul. 2015.
[21] T. Wu, C. Chang, L. Lin, G. Yu, and Y. Chang, "A D-Σ digital control for three-phase inverter to achieve active and reactive power injection," *IEEE Trans. Ind. Electron.*, vol. 61, no. 8, pp. 3879–3890, Aug. 2014.
[22] Y. Chang, S. Wang, W. Dai, and H. Chang, "Division-summation current control and one-cycle voltage regulation of the surface-mounted permanent-magnet synchronous generator," *IEEE Trans. Power Electron.*, vol. 31, no. 2, pp. 1391–1400, Feb. 2016.
[23] T. Wu, H. Hsieh, C. Hsu, and Y. Chang, "Three-phase three-wire active power filter with D-Σ digital control to accommodate filter-inductance variation," *IEEE J. Emerg. Sel. Topics Power Electron.*, vol. 4, no. 1, pp. 44–53, Mar. 2016.
[24] T. Wu, P. Lee, L. Lin, C. Chang, and Y. Chen, "Circulating current reduction for three-phase back-to-back transformerless inverter with SPWM-based D-Σ digital control," *IEEE Trans. Power Electron.*, vol. 32, no. 2, pp. 1591–1601, Feb. 2017.
[25] T.-F. Wu, T.-C. Chou, C.-W. Huang, and K. Sun, "Bi-directional grid-connected modular multilevel converters with direct digital control and D-Σ processes," *IEEE Trans. Power Electron.*, vol. 34, no. 11, pp. 11290–11299, Nov. 2019.
[26] T.-F. Wu, L.-C. Lin, C.-H. Chang, and P.-H. Lee, "Filter-capacitor current compensation for D-Σ digital controlled single-phase bi-directional inverter with LCL filter to reduce grid-current distortion," in *Proc. IEEE Appl. Power Electron. Conf. Expo.*, 2014, pp. 2259–2263.
[27] Y. He, X. Wang, X. Ruan, D. Pan, and K. Qin, "Hybrid active damping combining capacitor current feedback and point of common coupling voltage feedforward for LCL-type grid-connected inverter," *IEEE Trans. Power Electron.*, vol. 36, no. 2, pp. 2373–2383, Feb. 2021.
[28] C. Bao, X. Ruan, X. Wang, W. Li, D. Pan, and K. Weng, "Step-by-step controller design for LCL-type grid-connected inverter with capacitor–current-feedback active-damping," *IEEE Trans. Power Electron.*, vol. 29, no. 3, pp. 1239–1253, Mar. 2014.
[29] J. R. Massing, M. Stefanello, H. A. Grundling, and H. Pinheiro, "Adaptive current control for grid-connected converters with LCL filter," *IEEE Trans. Ind. Electron.*, vol. 59, no. 12, pp. 4681–4693, Dec. 2012.
[30] Y. He, H. S. Chung, C. Lai, X. Zhang, and W. Wu, "Active cancelation of equivalent grid impedance for improving stability and injected power quality of grid-connected inverter under variable grid condition," *IEEE Trans. Power Electron.*, vol. 33, no. 11, pp. 9387–9398, Nov. 2018.
[31] X. Lin, J. Yu, R. Yu, J. Zhang, Z. Yan, and H. Wen, "Improving small-signal stability of grid-connected inverter under weak grid by decoupling phase-lock loop and grid impedance," *IEEE Trans. Ind. Electron.*, vol. 69, no. 7, pp. 7040–7053, Jul. 2022.
[32] M. Li, H. Xiao, and M. Cheng, "An adaptive strategy based on repetitive predictive control for improving adaptability of LCL-type grid-connected inverters under weak grid," *IEEE Trans. Power Electron.*, vol. 37, no. 3, pp. 2562–2572, Mar. 2022.
[33] M. Cespedes and J. Sun, "Adaptive control of grid-connected inverters based on online grid impedance measurements," *IEEE Trans. Sustain. Energy*, vol. 5, no. 2, pp. 516–523, Apr. 2014.
[34] T. Roinila, T. Messo, and E. Santi, "MIMO-identification techniques for rapid impedance-based stability assessment of three-phase systems in DQ domain," *IEEE Trans. Power Electron.*, vol. 33, no. 5, pp. 4015–4022, May 2018.
[35] T. Roinila, M. Vilkko, and J. Sun, "Online grid impedance measurement using discrete-interval binary sequence injection," *IEEE J. Emerg. Sel. Topics Power Electron.*, vol. 2, no. 4, pp. 985–993, Dec. 2014.
[36] N. Hoffmann and F. W. Fuchs, "Minimal invasive equivalent grid impedance estimation in inductive–resistive power networks using extended Kalman filter," *IEEE Trans. Power Electron.*, vol. 29, no. 2, pp. 631–641, Feb. 2014.
[37] T. Fang, X. Zhang, C. Huang, W. He, L. Shen, and X. Ruan, "Control scheme to achieve multiple objectives and superior reliability for input-series-output-parallel LCL-type grid-connected inverter system," *IEEE Trans. Ind. Electron.*, vol. 67, no. 1, pp. 214–224, Jan. 2020.
[38] D. Yang, X. Ruan, and H. Wu, "Impedance shaping of the grid-connected inverter with LCL filter to improve its adaptability to the weak grid condition," *IEEE Trans. Power Electron.*, vol. 29, no. 11, pp. 5795–5805, Nov. 2014.
[39] J. W. Fattaruso, "New graphical tools for visualizing the Laplace and z-domains," *IEEE Circuits Syst. Mag.*, vol. 17, no. 3, pp. 17–31, Jul.–Sep. 2017.
[40] J. A. Suul, M. Molinas, L. Norum, and T. Undeland, "Tuning of control loops for grid connected voltage source converters," in *Proc. IEEE 2nd Int. Power Energy Conf.*, 2008, pp. 797–802.
[41] X. Li and R. Kennel, "General formulation of Kalman-filter-based online parameter identification methods for VSI-fed PMSM," *IEEE Trans. Ind. Electron.*, vol. 68, no. 4, pp. 2856–2864, Apr. 2021.
[42] N. Hoffmann and F. W. Fuchs, "Minimal invasive equivalent grid impedance estimation in inductive–resistive power networks using extended Kalman filter," *IEEE Trans. Power Electron.*, vol. 29, no. 2, pp. 631–641, Feb. 2014.
[43] B. Ren, X. Sun, M. Yu, J. Liu, and Q. Zhang, "Circulating current analysis and the improved D-Σ digital control strategy for multiparalleled three-level T-type grid-connected inverters," *IEEE Trans. Ind. Electron.*, vol. 67, no. 4, pp. 2810–2821, Apr. 2020.

Jiang Liu received the B.S. degree in electrical engineering from Xi'an University of Technology, Xi'an, China, in 2015, and the M.S. degree in electrical machinery and appliances in electrical engineering from the Xi'an University of Technology, Xi'an, China, in 2018, where he is working toward the Ph.D. degree in power electronics and electrical drive since 2018.

His research interests includes photovoltaic grid connected inverters, matrix converter and the control of bidirectional power converter.

Xiangdong Sun (Member, IEEE) was born in Shenyang, China, in 1971. He received the Ph.D. degree in electrical engineering from Xi'an University of Technology, Xi'an, China, in 2003.

During 2006–2008, he was a postdoctoral researcher with Tokyo Polytechnic University, supported by the government scholarship of Japan. Since 2009, he has been with the Department of Electrical Engineering, Xi'an University of Technology, where he is currently a Professor. His research interests include motor control, power electronics, and renewable energy systems.

Biying Ren was born in Henan, China, in 1971. She received the B.Sc., M.Sc., and Ph.D. degrees in electrical engineering from Xi'an University of Technology, Xi'an, China, in 1995, 2001, and 2009, respectively.

Since 1998, she has been with the Department of Electrical Engineering, Xi'an University of Technology, where she is currently an Associate Professor. Her research interests include renewable energy systems and microgrid operation systems.

Weizhang Song was born in Henan province, China, in 1980. He received the B.S. and M.S. degrees in information and control engineering and the Ph.D. degree in electrical engineering from Xi'an University of Technology, Xi'an, China, in 2004, 2007, and 2010, respectively.

In 2011, he joined the Department of Xi'an University of Technology, where he became an Associate Professor in 2014. From 2014 to 2015, he was a Research Fellow (Postdoctoral Fellow) with the Power Electronics, Machines and Control Group, University of Nottingham, Nottingham, U.K. His research interests include power electronics and ac drive systems, especially matrix converters and VIENNA rectifiers.

Patrick Wheeler (Fellow, IEEE) received the B.Eng. (Hons.) degree in electrical engineering and the Ph.D. degree in electrical engineering (for the work on matrix converters) from the University of Bristol, Bristol, U.K., in 1990 and 1994, respectively.

In 1993, he moved to the University of Nottingham, Nottingham, U.K., and was a Research Assistant with the Department of Electrical and Electronic Engineering. In 1996, he became a Lecturer with the Power Electronics, Machines and Control Group, University of Nottingham. Since January 2008, he has been a Full Professor with the same research group. From 2015 to 2018, he was the Head of the Department of Electrical and Electronic Engineering, University of Nottingham. He is currently the Head of the Power Electronics, Machines and Control Group and Global Director of the University of Nottingham's Institute of Aerospace Technology, and was the Li Dak Sum Chair Professor in electrical and aerospace engineering. He authored or coauthored more than 750 academic publications in leading international conferences and journals.